The Journal of Chemical Physics

Bonding in nitrile photo-dissociating ruthenium drug candidates—A local vibrational mode study

Cite as: J. Chem. Phys. **157**, 014301 (2022); https://doi.org/10.1063/5.0094567
Submitted: 04 April 2022 • Accepted: 10 June 2022 • Accepted Manuscript Online: 13 June 2022 • Published Online: 01 July 2022

Margaret McCutcheon, Marek Freindorf and Elfi Kraka

The Journal of Chemical Physics ARTICLE scitation.org/journal/jcp

Bonding in nitrile photo-dissociating ruthenium drug candidates—A local vibrational mode study

Cite as: J. Chem. Phys. **157**, 014301 (2022); doi: 10.1063/5.0094567
Submitted: 4 April 2022 • Accepted: 10 June 2022 •
Published Online: 1 July 2022

Margaret McCutcheon, Marek Freindorf, and Elfi Kraka[a)]

AFFILIATIONS

Department of Chemistry, Southern Methodist University, Dallas, Texas 75205, USA

Note: This paper is part of the JCP Special Topic on Nature of the Chemical Bond.
[a)]**Author to whom correspondence should be addressed:** ekraka@smu.edu

ABSTRACT

In this work, we investigated bonding features of 15 ruthenium(II) nitrile complexes of the type $[Ru(tpy)(L)\text{-}(CH_3CN)]^{n+}$, containing the tridentate tpy ligand (tpy = 2,2′:6′,2″-terpyridine) and various bidentate ancillary ligands L; 12 compounds originally synthesized by Loftus *et al.* [J. Phys. Chem. C **123**, 10291–10299 (2019)] and three new complexes. We utilized local vibrational force constants derived from the local mode theory as a quantitative measure of bond strength complemented with the topological analysis of the electron density and the natural bond orbital analysis. Loftus *et al.* suggested that nitrile dissociation occurs after light induced singlet–triplet transition of the original complexes and they used as a measure of nitrile release efficiency quantum yields for ligand exchange in water. They observed larger quantum yields for complexes with smaller singlet–triplet energy gaps. The major goal of this work was to assess how the Ru–NC and Ru–L bond strengths in these 15 compounds relate to and explain the experimental data of Loftus *et al.*, particularly focusing on the question whether there is a direct correlation between Ru–NC bond strength and measured quantum yield. Our study provides the interesting result that the compounds with the highest quantum yields also have the strongest Ru–NC bonds suggesting that breaking the Ru–NC bond is not the driving force for the delivery process rather than the change of the metal framework as revealed by first results of a unified reaction valley approach investigation of the mechanism. Compounds with the highest quantum yield show larger electronic structure changes upon singlet–triplet excitation, i.e., larger changes in bond strength, covalency, and difference between the singlet and triplet HOMOs, with exception of the compound 12. In summary, this work provides new insights into the interplay of local properties and experimental quantum yields forming in synergy a useful tool for fine tuning of existing and future design of new nitrile releasing ruthenium compounds. We hope that this work will bring theoretical and experimental studies closer together and serves as an incubator for future collaboration between computational chemists and their experimental colleagues.

I. INTRODUCTION

Cancer, the uncontrolled growth of cells, is one of the most well-known diseases plaguing mankind. In the later stages, a cancer diagnosis is often a death sentence due to the inability of the human body to tolerate the necessary chemotherapeutic chemicals. Current-generation chemotherapy drugs rely strongly on a platinum ion to twist DNA during the metaphase of cell growth.[1] However, next generation cancer treatments incorporate a ruthenium (II) ion, which has many desirable properties compared to platinum. Particularly relevant are drugs currently undergoing clinical trials—NKP1339, NAMI-A, RM175, and RAPTA-C.[1–3] Such drugs are preferable to platinum based chemotherapies due to their cytotoxicity against cisplatin resistant cells and their higher selectivity toward tumor cells.[4] These ruthenium-based drugs exhibit a variety of complex geometries. Arene half-sandwich complexes provide methods of linking arenes such as *p-cymene* groups[5–8] and benzene groups to a ruthenium center and then adding a releasable cytotoxic component, such as diphosphanes,[5] triazole,[7] hydrozone,[6] or a glutathione *S*-transferase inhibitor.[9] In addition, piano-stool geometries have been shown to be effective in treating cancer through anti-proliferative effects.[10,11] Rafols *et al.*[12] have recently reported the synthesis of piano-stool ruthenium compounds showing excellent cytotoxicity after incubation in aged dimethyl sulfoxide (DMSO). Yet another unique geometry synthesized by da Silva *et al.*[13] has shown cytotoxic properties through the inhibition of topoisomerase IB. Gupta *et al.*[14] have synthesized acetylacetone ruthenium complexes that induce apoptosis and are of particular interest due to

their lipophilicity and associated cell delivery. As the library of these ruthenium based compounds grows, the scientific community has observed the effectiveness of ruthenium (II) complexes deriving from a variety of properties unique to the metal.

Due to ruthenium's and iron's similar electronic structure, ruthenium compounds are able to undergo active transport into the cell via iron transporters.[4,15,16] This also accounts for the selectivity of ruthenium based compounds toward tumor cells, as cancerous cells up-regulate the intake of iron to proliferate. Ruthenium compounds have been shown to accumulate inside the mitochondria and endoplasmic reticulum to inhibit kinase pathways.[4,17] The most important properties of ruthenium complexes, however, are their favorable adsorption properties, photochemical, and photophysical properties,[18–20] making them promising candidates for photoactive metalloantibiotics[21,22] and photo-chemotherapy, where the drugs become activated after receiving visible light irradiation of the tumor *in vivo*,[23–29] again so far mostly relying on platinum based drugs.[30]

Ruthenium's properties as a transition metal are what makes it so important in the search for next-generation chemotherapeutics.[31,32] It exhibits five oxidation states with (II) and (III) being the most common[33] and typically forms six coordinations. These coordination complexes are typically formed with polypyridines and exhibit long-lived excited states[34] though not all excited states are accessible.[35] This characteristic is explained by the mixing of the ruthenium d orbitals and the ligand's π and π^* orbitals.[36] Arene-coordinated complexes can be synthesized to show a considerable gap between the ground state and the metal-centered (MC) state.[37,38] Exploiting the nature of this energy gap is key to the development of photo-dissociative drugs. Metal-to-ligand-charge-transfer (MLCT) allows for a charge to be moved from ruthenium to one of the coordinated ligands.

Polypyridyl ruthenium (II) complexes that have been involved so far in a wide range of applications ranging from solar energy,[39] molecular switches,[40,41] and biological sensors[42,43] to photo-redox catalysis[35,44] show also a high potential as photo-activated chemotherapeutic. Upon irradiation of light, electronic excitation of the singlet ground state of the polypyridyl ruthenium (II) complex takes place followed by intersystem crossing to a lower lying excited triplet state out of which ligand dissociation for the controlled release of DNA binding drugs, kinase inhibitors, or other cytotoxic reagents occurs, which qualifies these compounds as potential drug delivery systems.[29,45–49] Loftus *et al.* synthesized 12 ruthenium (II) complexes of the type $[Ru(tpy)(L)\text{-}(CH_3CN)]^{n+}$, containing the tridentate tpy ligand (tpy = 2,2′:6′,2″-terpyridine), various bidentate ancillary ligands L, shown in Fig. 1(a), and the methyl nitrile group as a model for nitrile-based drugs.[28] They found that these complexes are stable in the dark but absorb light throughout the visible range and form long-lived excited triplet states out of which nitrile dissociation occurs as depicted in Fig. 1(b), leading to a five-coordinated Ru(II) triplet intermediate. After relaxation to the singlet state, the association of a water molecule from the aqueous environment follows, filling the empty Ru coordination site. As a measure of drug release efficiency, these authors suggested recorded quantum yields (QY) for water association. In addition to QYs, they derived singlet–triplet splitting energy differences (ST) for the original ruthenium (II) complexes **1**–**12** from emission spectra taken at 77 K. Two distinct groups emerged from their study—Group 1 complexes **1**–**7** with larger STs and lower QYs, i.e., drug delivery

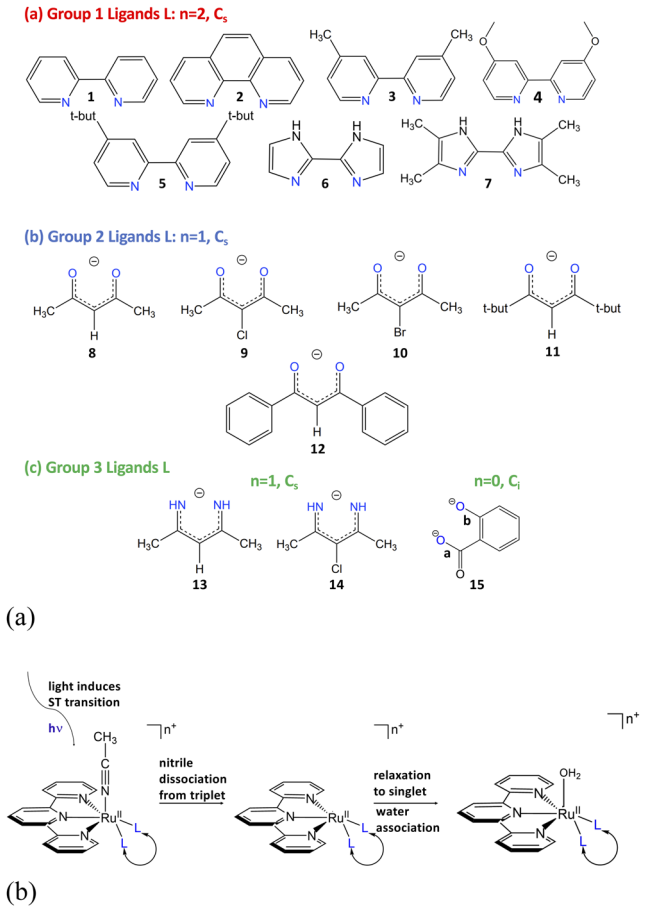

FIG. 1. (a) Schematic of the different ruthenium(II) ligands L investigated in this work. Group 1 and Group 2: ligands suggested in Ref. 28; Group 3: new ligands suggested in this work. (b) General scheme of Ru(II) complexes investigated in this work and overall mechanism leading to water association suggested in Ref. 28.

efficiencies (shown in red in Fig. 2), and Group 2 complexes **8**–**11** with smaller STs and higher QYs, i.e., drug delivery efficiencies (shown in blue in Fig. 2 and one outlier), **12** with an ST splitting comparable to that of other Group 2 members but with the smallest overall QY found in their study.[28] In the following work, Loftus *et al.*[50] provided evidence that the population of triplet ligand field (^{3}LF) excited states[51–53] is not necessary for photo-induced nitrile dissociation based on their finding that compounds with the greatest QYs have the longest ^{3}MLCT excited state lifetimes, i.e., they are less able to populate the dissociative (^{3}LF) states.

Intrigued by the Loftus proposal, we explored in this work the question if the QYs, which assess the drug release efficiency in a holistic way via monitoring ligand exchange correlate with local measures, in particular the strength of the ruthenium–nitrile (Ru–NC) bond, and how different ruthenium-ancillary ligands L influence the Ru–NC bond strength, with the overall goal to develop a protocol for fine-tuning drug release efficiencies of these complexes based on Ru–CN and Ru–L bond properties. We utilized

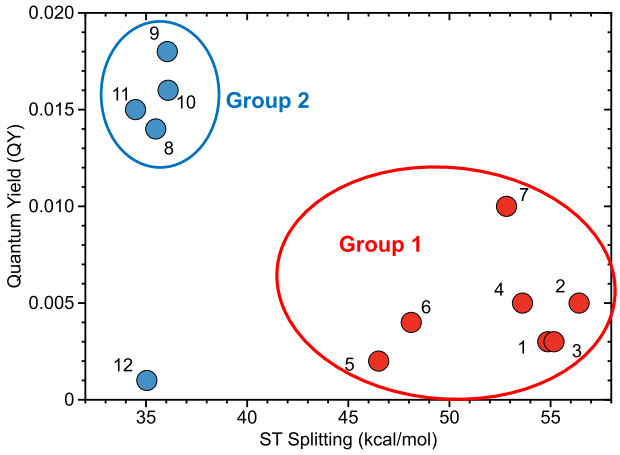

FIG. 2. Experimental QYs for water association taken from Ref. 28 vs calculated ST splittings (defined as the energy difference between the first excited triplet state and the ground state singlet). (PBE0/cc-pVTZ/SDD level of theory.)

local vibrational stretching force constants k^a derived from the local mode analysis (LMA) developed in our group.[54] LMA was complemented with the topological analysis of the electron density using Bader's quantum theory of atoms-in-molecule (QTAIM)[55–58] and the natural orbital (NBO) analysis[59,60] to round up our bonding analysis.

Based on preliminary results and recent literature,[61,62] we added three novel complexes **13**–**15** to the original Loftus set [i.e., Group 3, see Fig. 1(a)] as potential candidates with increased drug release efficiency.

This manuscript is structured in the following way: first, computational methods applied in this work are summarized, followed by a discussion of our results. Then, some conclusions are drawn, and work in progress is highlighted.

II. COMPUTATIONAL METHODS

As a quantitative measure of bond strength for the Ru–NC and Ru–L bonds investigated in this work, we used local vibrational force constants k^a derived from LMA, which is based on vibrational spectroscopy. The theoretical background of LMA, originally developed by Konkoli and Cremer,[63–67] can be found in a comprehensive review article.[54] The local vibrational modes of a molecule are the local counterparts of normal vibrational modes, which are generally delocalized due to electronic and mass-coupling.[68] Therefore associated normal mode stretching force constants are of limited use as individual bond strength descriptors. In contrast, local vibrational stretching force constants derived from uncoupled local vibrational modes directly reflect the intrinsic strength of a chemical bond and/or weak chemical interaction.[69] We have successfully applied local stretching force constants to characterize covalent bonds[69–75] and weak chemical interactions, such as halogen bonds,[76–81] chalcogen bonds,[82–84] pnicogen bonds,[85–87] tetrel bonds,[88] and hydrogen bonds,[89–97] as well as so-called π-hole interactions.[98]

It is convenient to compare the bond strengths in a series of compounds using a bond strength order (BSO), rather than comparing the local force constant values. These properties are related via a power relationship according to a generalized Badger rule derived by Kraka *et al.*,[71]

$$BSO = a(k^a)^b. \quad (1)$$

The constants a and b in Eq. (1) can be determined via two reference compounds with known k^a and the requirement that the BSO is zero for a zero force constant. In our study, the power relation between k^a and BSO [Eq. (1)] has been based on two reference molecules, RuH and RuO, for which we calculated Mayer's bond orders at the PBE0/cc-pVTZ/SDD level of theory leading to values of 0.9373 and 1.4812 for RuH and RuO, respectively. By scaling Mayer's bond order of RuH to 1.0, the scaled value of Mayer's bond order of RuO was 1.5803. Local mode force constants k^a at the same level of theory for RuH and RuO are 2.143 and 6.978 mdyn/A, respectively, which led to the power relation coefficients a = 0.7441 and b = 0.3879, applied throughout this work.

The covalent character of the Ru–NC and Ru–L bonds was assessed via the Cremer–Kraka criterion,[99,100] which is based on the value of the energy density H_b taken at the bond critical point $\mathbf{r}_b$ on the electron density bond path between the two atoms involved in the chemical bond or weak chemical interaction.[55–58] A negative value of H_b indicates the covalent character of the bond/interaction, whereas a positive value reflects the dominant electrostatic character. The NBO analysis[59,60,101] was applied to explore the role of Ru d-orbital contributions to bonding.

Density Functional Theory (DFT)[102–105] was used for all geometry optimizations, frequency calculations, and wave function analyses performed in this study. All calculations were carried out with the PBE0[106] hybrid functional, which has been found to produce experimentally accurate geometries for ruthenium tetracarbonyl polymers[107] and methylimidazole complexes.[108] We used this functional in combination with the Dunning and Kendall's cc-pVTZ basis set.[109] In order to account for relativistic effects for ruthenium, the Stuttgart–Dresden effective core potential (SDD) was applied, which is a quasi-relativistic *ab initio* pseudo-potential substituting the $M(Z\text{-}28)^+$ core orbitals of the second row transition elements, used together with the corresponding optimized GTO valence basis set and with the corresponding spin–orbit coupling operator.[110,111] This model chemistry is comparable to that used by Loftus *et al.* (PBE/def2-TZVP/SDD),[28] but the cc-pVTZ basis set is larger and more flexible,[109,112] containing more basis functions per atom and has been found to have higher accuracy in accounting for relativistic effects and effective core potentials.[113] A comparison of theoretically calculated bond lengths compared with those obtained from x-ray crystallography by Loftus and co-workers depicts a linear correlation between experimental and theoretical values obtained at the PBE0/cc-pVTZ/SDD (Ru) level of theory (see Fig. S1 of the supplementary material). The harmonic normal vibrational frequencies of the Ru–NC bonds (449–502 cm^{-1}) in Ru–Npy compounds with a second phenyl ligand bound to the ruthenium reported by Garza-Ortiz *et al.*[114] cover about the same range as our harmonic local vibrational frequencies (see Table S1 of the supplementary material), showing the dominant Ru–CN character of these modes. The Cartesian coordinates and symmetries of

the geometry optimized complexes **1**–**15** (singlet and triplet states), the corresponding complexes after nitrile dissociation (singlet and triplet states), and the complexes with the associated water ligand (only calculated in their singlet state) are collected in Tables S4–S6 of the supplementary material. For the triplet state calculations, unrestricted DFT was applied,[115] and, for all DFT calculations, an ultrafine integral grid was used.[116] DFT calculations were carried out with Gaussian 16.[117] The local mode force constants were calculated with the LMODEA package.[118] The electron density analysis was performed with the AIMAll program,[119] and Mayer bond orders were calculated with Gaussian 16.[117] NBO Ru d-orbital occupations of HOMO and LUMO orbitals were determined with the program NBO6.[120]

III. RESULTS AND DISCUSSION

This section is structured in the following way: in Sec. III A, the bond strength of the Ru–NC and Ru–L bonds and their relationship are analyzed. In Sec. III B, these results are discussed in the context of nitrile release and water association, including a comparison with the experimental QY's of Loftus *et al.*,[28] and in Sec. III C, first mechanistic studies on the nitrile release are presented.

In Table I, calculated Ru–NC and Ru–L bond lengths R (Å), local mode force constants k^a (mdyn/Å), and corresponding bond strength orders BSO, electron density ρ_b (e/Å^3), and energy density H_b (hartree/Å^3) at the bond critical point **b** are collected for complexes **1**–**15**. Figure 3 shows the corresponding BSO plots, Fig. 4

TABLE I. Bond length R (Å), local mode force constant k^a (mdyn/Å), bond strength order BSO, electron density ρ_b (e/Å^3), and energy density H_b (hartree/Å^3) at the bond critical point **b** for complexes **1**–**15**. PBE0/cc-pVTZ/SDD level of theory.

	Singlet					Triplet				
Complex	R	k^a	BSO	ρ_b	H_b	R	k^a	BSO	ρ_b	H_b
					Ru–CN bond					
1	2.020	1.395	0.846	0.099	−0.149	2.065	1.395	0.847	0.092	−0.130
2	2.017	1.624	0.898	0.100	−0.153	2.044	1.514	0.874	0.097	−0.152
3	2.019	1.607	0.894	0.099	−0.151	2.046	1.496	0.870	0.097	−0.149
4	2.016	1.627	0.899	0.100	−0.153	2.043	1.544	0.881	0.097	−0.151
5	2.019	1.619	0.898	0.100	−0.151	2.041	1.444	0.858	0.098	−0.152
6	2.006	1.718	0.918	0.103	−0.164	2.023	1.581	0.889	0.102	−0.170
7	2.003	1.711	0.916	0.104	−0.166	2.031	1.605	0.894	0.100	−0.164
8	1.985	1.852	0.945	0.109	−0.194	2.013	1.557	0.883	0.104	0.000
9	1.985	1.857	0.946	0.109	−0.194	2.010	1.576	0.888	0.104	−0.175
10	1.985	1.856	0.946	0.109	−0.194	2.010	1.576	0.888	0.104	−0.175
11	1.985	1.842	0.943	0.109	−0.193	2.014	1.544	0.881	0.103	−0.171
12	1.985	1.8490	0.944	0.109	−0.194	2.011	1.561	0.884	0.104	−0.173
13	2.019	1.571	0.887	0.100	−0.154	2.056	1.239	0.809	0.092	−0.124
14	2.019	1.573	0.887	0.100	−0.153	2.057	1.231	0.807	0.092	−0.123
15	1.994	1.713	0.917	0.108	−0.195	2.030	1.340	0.834	0.099	−0.157
					Ru–L bond					
1	2.087	1.969	0.968	0.102	−0.187	2.009	2.414	1.047	0.115	−0.260
2	2.086	1.710	0.916	0.092	−0.146	2.008	1.535	0.879	0.989	−0.183
3	2.064	1.814	0.937	0.094	−0.155	2.078	1.670	0.908	0.101	−0.192
4	2.098	1.821	0.939	0.092	−0.149	2.047	1.961	0.966	0.100	−0.187
5	2.063	2.014	0.976	0.102	−0.190	2.054	2.030	0.979	0.108	−0.220
6	2.082	1.653	0.904	0.095	−0.157	2.067	1.589	0.890	0.101	−0.187
7	2.111	1.466	0.863	0.081	−0.109	2.074	1.615	0.896	0.091	−0.150
8	2.044	1.746	0.924	0.083	−0.070	2.009	1.902	0.955	0.097	−0.135
9	2.073	2.085	0.989	0.093	−0.103	2.025	1.985	0.971	0.103	−0.103
10	2.070	1.829	0.940	0.084	−0.070	2.074	1.976	0.969	0.099	−0.146
11	2.038	1.813	0.937	0.084	−0.076	2.003	1.971	0.968	0.099	−0.143
12	2.073	1.792	0.933	0.084	−0.075	2.019	1.561	0.884	0.100	−0.144
13	2.071	2.025	0.978	0.099	−0.179	1.985	2.361	1.038	0.120	−0.268
14	2.063	2.108	0.994	0.101	−0.185	1.975	2.346	1.036	0.119	−0.263
15-La	2.049	2.101	0.992	0.093	−0.113	2.020	1.755	0.925	0.101	−0.149
15-Lb	2.008	2.426	1.049	0.106	−0.170	1.952	2.243	1.018	0.122	−0.237

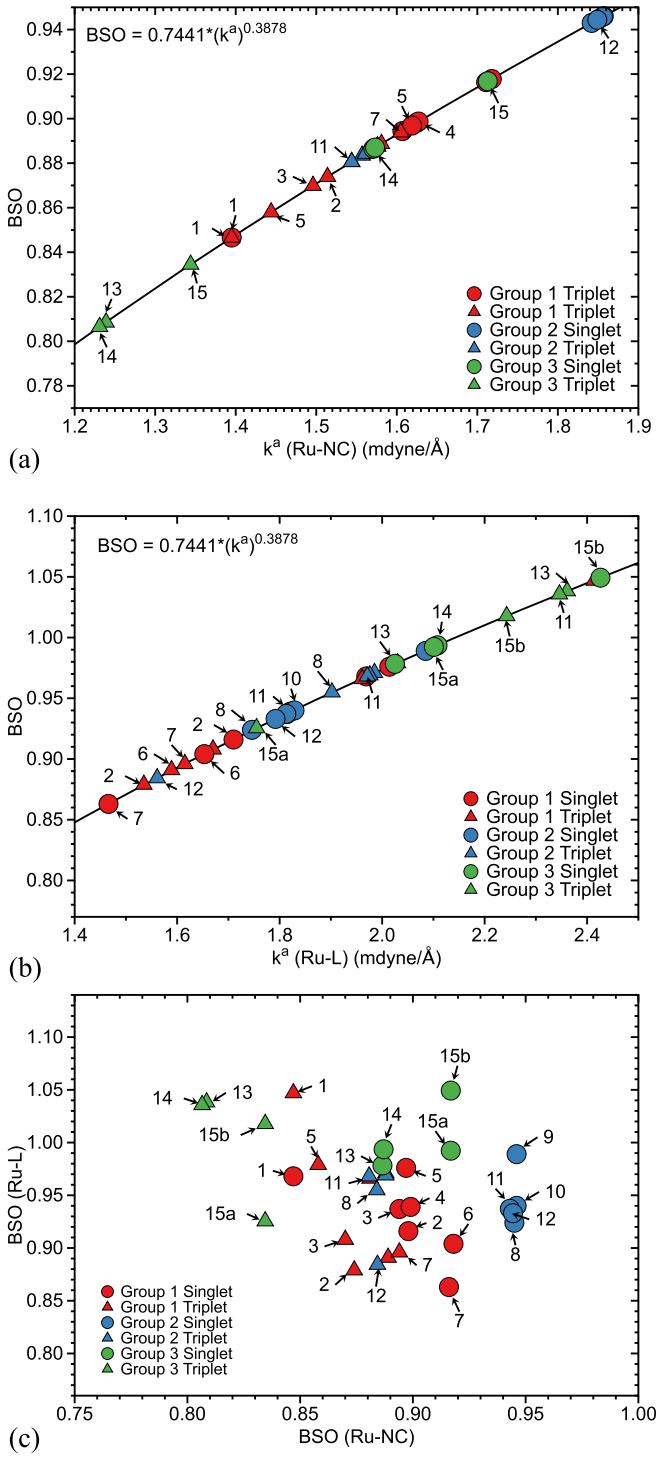

FIG. 3. (a) BSO values of all Ru–NC bonds (singlet and triplet states) and (b) BSO values of all Ru–L bonds (singlet and triplet states) obtained with the power relationship BSO = 0.7441 $(k^a)^{0.3879}$, calculated at the PBE0/cc-pVTZ/SDD level of theory. See text and Eq. (1) for the derivation of the power relationship. (c) Comparison of Ru–NC to Ru–L BSO values. Group 1 compounds **1**–**7** in red, Group 2 compounds **8**–**12** in blue, and Group 3 compounds **13**–**15** in green.

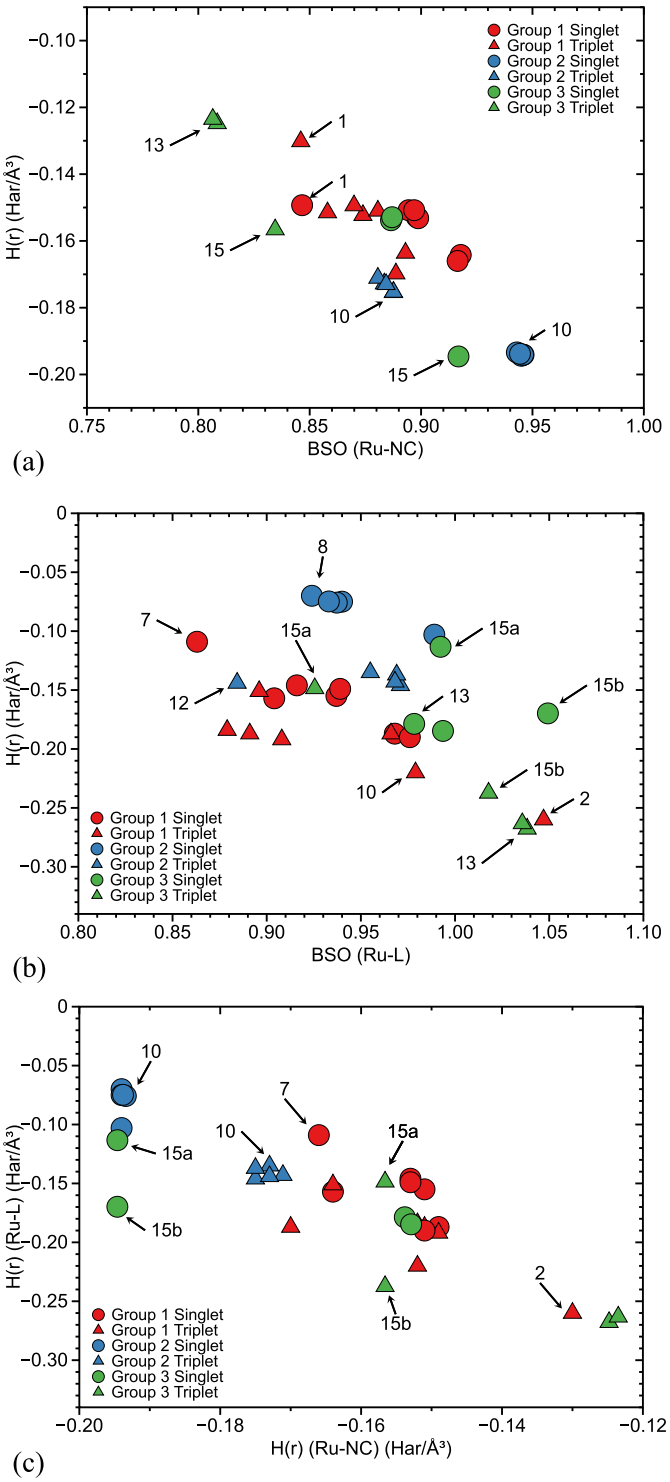

FIG. 4. Correlation between energy density H_b and BSO (a) for Ru–NC bonds (singlet and triplet states) and (b) for Ru–L bonds (singlet and triplet states) calculated at the PBE0/cc-pVTZ/SDD level of theory. (c) Correlation between H_b(Ru–NC) and H_b(Ru–L). Group 1 compounds **1**–**7** in red, Group 2 compounds **8**–**12** in blue, and Group 3 compounds **13**–**15** in green.

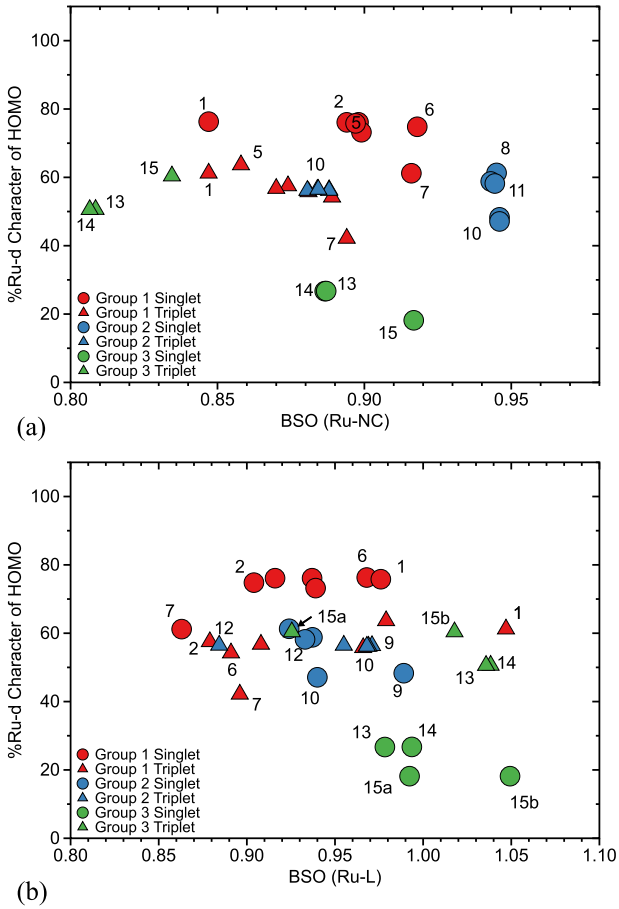

FIG. 5. Comparison of Ru–NC BSO with the percentage contribution of Ru-d character to the HOMO. Ru–NC BSO vs Ru-d character of the singlet HOMO (a); Ru–NC BSO vs Ru-d character of the triplet HOMO (b); Ru–NC vs Ru-d character of the HOMO, both singlet and triplet. PBE0/cc-pVTZ/SDD level of theory.

shows the corresponding H_b plots for the Ru–NC and Ru–L bonds, and Fig. 5 focuses on the Ru d-orbital occupations of HOMO orbitals.

A. Bond analysis

As revealed from the data in Table I and Fig. 3(a), the strength of the ruthenium–nitrile bonds covers a range between 0.80 and 0.95 (including complexes in their singlet and triplet states). Interesting to note is that the strongest Ru–NC bonds of complexes in their singlet state are found for Group 2 members (BSO values of 0.943–0.946) compared with Group 1 members (BSO values of 0.846–0.916) and Group 3 members (BSO values of 0.887–0.917). We observe the general trend that upon excitation from singlet to triplet state, the Ru–NC bond becomes weaker (see BSO differences in Table S2 of the supplementary material). Interesting to note is that the Ru–NC bond weakening upon ST excitation is most pronounced for Group 2 and Group 3 members with Δ[BSO(T) − BSO(S)] values in the 0.06 range for Group 2 and in the 0.08 range for Group 3, relating increased QYs to larger changes of the Ru–NC bonds. The data in Table I and Fig. 3(b) show a bond strength range between 0.86 and 1.05 for the Ru–L bonds. In contrast to the Ru–NC bond, there is no uniform bond weakening trend for the Ru–L bond upon ST excitation, as reflected by the BSO differences in Table S2 of the supplementary material. Some Ru–L bonds are weaker in their singlet state than in their triplet state, and for others, the opposite is true. Overall, Δ[BSO(T) − BSO(S)] values vary between −0.8 and 0.7.

Figure 3(c) depicts the relationship between the BSO values of Ru–NC and Ru–L bonds. Although there is no significant correlation between the strength of the ruthenium nitrile bond and that of the ruthenium ancillary ligand bond, there is a trend that to some extent a weaker Ru–L bond corresponds to a stronger Ru–NC bond. A more strongly associated ancillary ligand siphons electron density from the Ru–NC bond, thus weakening it. We also observe several groupings in Fig. 3(c) among the singlet and triplet states of compounds **8**–**11** and the triplet states of **1**–**7** and **12**. In comparing the triplet states of **8**–**11** with the singlet states, the Ru–NC bond is weakened while Ru–L is strengthened. This is consistent with the chemical thinking that in the triplet state, electron density moves out of the Ru–NC bond toward the ancillary ligand, thus accounting for the photo-dissociation of the compound. This difference is even more pronounced in our proposed compounds **13** and **14**. These compounds show an increase in Ru–L strength with a simultaneous decrease in Ru–NC. Most interesting in this context is that compound **12** has a lower QY than expected,[28] appearing in Fig. 1 as a clear outlier of Group 2. Our local mode analysis provides a rationale for that. During the singlet to triplet transition, both Ru–NC and Ru–L are weakened in compound **12**. The simultaneous weakening of both bonds in **12** suggests that the nitrile is unable to efficiently photo-dissociate lacking reorganization of electron density to the ancillary ligand, i.e., nitrile is not freed easily from the complex.

Figure 4 evaluates the covalent character of the Ru–NC and Ru–L bonds via the correlation between H_b and BSO. According to the Cremer–Kraka criterion[99,100] described above, we find that all Ru–NC and Ru–L bonds investigated in this work are of covalent character with H_b values in the range of −0.12 to −0.20 (hartree/Å^3) for Ru–NC bonds (see Table I and Fig. 4(a)] and a somewhat larger range of −0.07 to −0.28 (hartree/Å^3) for Ru–L bonds [see Table I and Fig. 4(b)]. In both cases, we find the trend that stronger bonds (larger BSO values) show more covalent character (more negative H_b values). Figure 4(c) shows the comparison of the H_b values of Ru–NC and Ru–L bonds, showing the trend that a more covalent Ru–L bond correlates with a less covalent Ru–NC bond. As with BSO comparisons, we observe that, in the case of Ru–NC bonds, the singlet states show more covalent character, whereas the opposite holds for the Ru–L bonds. For compounds **8**–**11**, this energy density difference between singlet and triplet states is larger than that for **1**–**10**, and it is most pronounced for compounds **13**–**15**. Thus, we predict that our proposed compounds will show greater rearrangement of energy density from Ru–NC to Ru–L and, therefore, greater photo-dissociation of the nitrile group.

Loftus *et al.*[28] emphasized in their work the potential role of the Ru-d orbitals; they concluded that greater ruthenium d-character of the singlet state HOMO is associated with a lower quantum yield for the water association. In our work, we explored if there is a relationship between the Ru-d character of the HOMO for both singlet and triplet states and the Ru–NC bond strength depicted in

Fig. 5(a) and between the Ru-d character of the HOMO for both singlet and triplet states and the Ru–L bond strength depicted in Fig. 5(b). As obvious from Fig. 5, for both Ru–NC and Ru–L bonds, there is no significant correlation between these two quantities but we do observe some trends and groupings of compounds. Group 2 compounds **8**–**11** (shown in blue, with the highest QYs for water association) have a Ru-d character between 40% and 60% in their singlet states. Group 1 compounds (shown in red, with smaller QYs) show the largest Ru-d character with values up to 80%. In contrast, our proposed compounds (**13**–**15**) (shown in green) have the smallest Ru-d character of the singlet HOMO with less than 20% Ru-d character found for compound **15**. Thus, we assert that these compounds will show greater quantum yields than the original Loftus compounds. Figure 5(b) shows the correlation between the Ru-d character of the HOMO for both singlet and triplet states and the Ru–L bond strength showing a similar trend than that found for the Ru–NC bonds; the largest Ru-d character of about 80% for Group 2 members in their singlet states, medium values of 60% for Group 1 compounds, and smallest Ru-d character in the 20% range for Group 3 compounds.

Examination of the HOMO and LUMO orbitals provides further insights into the patterns observed in the correlation between Ru-d character and bond strength. In the following, some representative examples are discussed. A complete set of HOMO and LUMO plots for compounds **1**–**15**, singlet and triplet states is compiled in the supplementary material (Figs. S5–S19).

HOMO and LUMO of compound **4** (triplet state) are shown in Fig. 6(a) as a representative of Group 1. The primary orbital contribution of the triplet HOMO comes from the Ru-d and the tpy ligand orbitals with no contribution from nitrile orbitals. The triplet LUMO of compound **4** is also predominantly localized on the tpy ligand. The same is observed for the other Group 1 members, **1**–**3** and **5**–**7** (see Figs. S5–S7 and S9–S11 of the supplementary material). Since the tpy ligand does not change across the compounds investigated in this work, this explains why there is no direct correlation between the triplet Ru-d character and the Ru–NC or Ru–L bond strength, as revealed in Fig. 5. Figure 6(b) shows HOMO and LUMO of compound **9** (triplet state), and Fig. 6(c) shows HOMO and LUMO of compound **12** (triplet state). Both are members of Group 2. However, there is a distinct difference. Figure 6(b) shows that the HOMO of **9** is predominantly localized on the auxiliary ligand but shifts toward the tpy ligand in the LUMO. This rearrangement of electron density upon excitation in the triplet state can be considered as a major factor for the increased quantum yield of **8**–**11**. However, as evident from Fig. 6(c), the HOMO LUMO pattern of compound **12** resembles the Group 1 pattern; therefore, the substantially lower QY of this Group 2 member clarifies this compound as an outlier. In Fig. 6(d), the singlet HOMO of compound **9** (left) is compared with that of compound **14** (right), a Group 3 member. The compound **9** HOMO is localized at the ancillary ligand L. It is this localization and lack of Ru-d character that Loftus *et al.*[28] have shown to be strongly correlated with the quantum yield. This also confirms the influence of ligand L on the nitrile release for **8**–**11**, which we used as a design tool for our compounds. As illustrated in Fig. 6(d), compound **14** shows the same localization of the singlet HOMO to the ancillary ligand, as is also found for the other Group 3 members (see Figs. S17–S19 of the supplementary material), i.e., our proposed compounds show the same

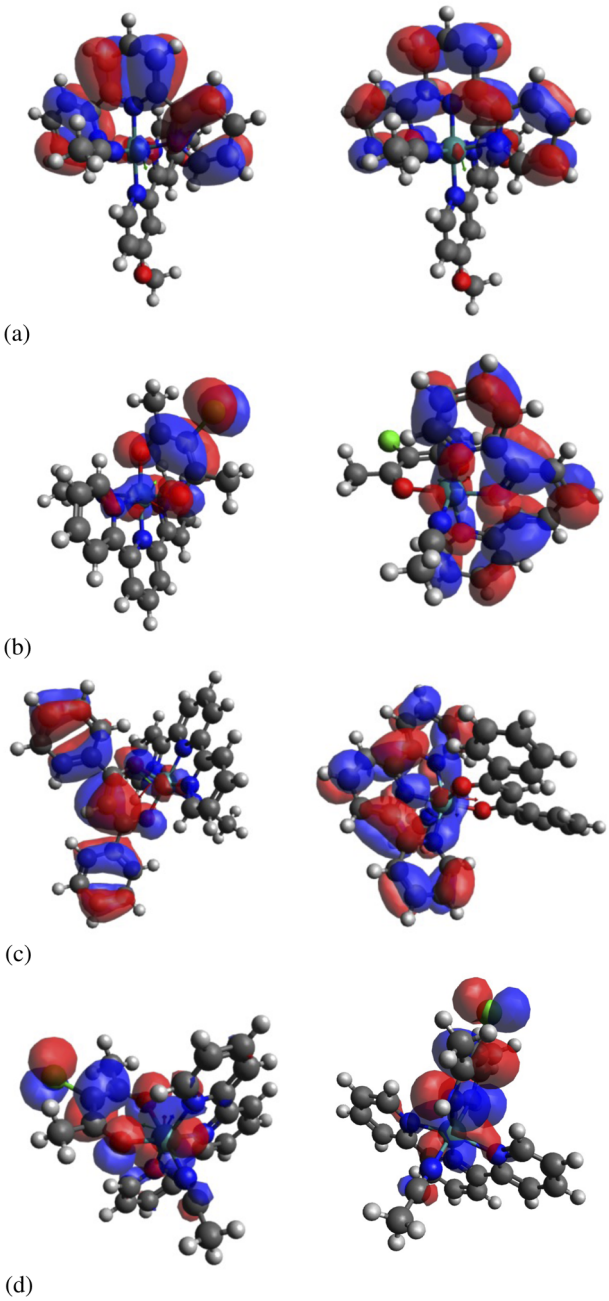

FIG. 6. Plots of the NBO HOMO and LUMO orbitals for select compounds: (a) compound **4** (triplet state, Group 1 member); (b) compound **9** (triplet state, Group 2 member); (c) compound **12** (triplet state, Group 2 member); and (d) singlet HOMO of compound **9** (left) and singlet HOMO of compound **14** (right, Group 3 member). PBE0/cc-pVTZ/SDD level of theory.

triplet HOMO/LUMO electron density redistribution as the most successful compounds synthesized by Loftus *et al.*,[28] adding another strong argument to the Ru-d orbital analysis for the potential of compounds **13**–**15** as a model for the fine-tuning and future design

of Ru(II) nitrile releasing drug candidates with modified auxiliary ligands.

B. Local vs global description of nitrile release

This section is devoted to the question if our local bond descriptors, particularly the Ru–NC correlate with the QYs of the water association, which was suggested by Loftus *et al.*[28] as an experimental measure of nitrile release. As illustrated in Fig. 1(b), the QYs are a holistic overall measure, resulting from several distinct reaction steps: (i) transition of the original six-coordinated Ru(II) complex into a long-lived triplet state upon exposure to light; (ii) nitrile release from the triplet state via the transformation into a five-coordinated Ru(II) complex; (iii) relaxation of the five-coordinated Ru(II) complex to the singlet state; and (iv) association of one water molecule and back-transformation into a six-coordinated Ru(II) complex. In Table II, the energetics for these steps are collected. The ST splitting energies (column one of Table II) cover a large range between 22 and 56 kcal/mol. As depicted in Fig. 2, QYs are related to the amount of energy needed to excite the original complex from the singlet to the triplet state, i.e., the lower the ST, the better the energy gap. With ST splitting energies in the range of 22 kcal/mol, compounds **13**–**15** have the lowest ST gaps, so we predict they will give high quantum yields, and are, therefore, valuable potential candidates to be explored by experiment.

Nitrile dissociation is an endothermic process for all 15 compounds, with smaller energy values for compounds **1**–**6** ranging from 7 to 14 kcal/mol. It is interesting to note that nitrile release of compound **7** is almost 55 kcal/mol most endothermic process found in our study, followed by Group 2 compounds with values in the 47 kcal/mol range. Group 3 compounds **13**–**15** show a large stretch from 20 to 40 kcal/mol.

Overall, it can be concluded that the endothermicity of the nitrile dissociation does not directly relate to the observed QYs,

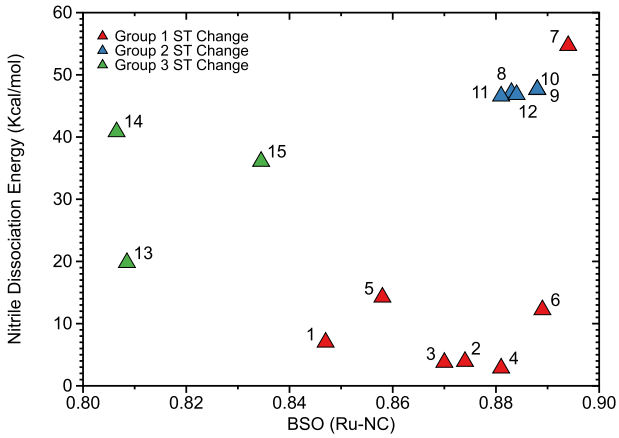

FIG. 7. Comparison of BSO (Ru–NC) bond strengths (triplet states) and nitrile dissociation energies. PBE0/cc-pVTZ/SDD level of theory.

and furthermore, there is no correlation between the Ru–NC bond strength and endothermicity of this process as shown in Fig. 7. Triplet to singlet (TS) relaxation is as expected exothermic for all compounds ranging from −8 to −18 kcal/mol and water association is even more exothermic with energies between −19 and −26 kcal/mol.

Energies and quantum yields describe a chemical process in a holistic and overall way, making it difficult to extract individual information or mechanistic details.[75,78,88,121–123] Therefore, in the following, we explore the interesting question if there is a correlation between local properties, particularly the Ru–NC bond strength and the observed quantum yields. Because the nitrile dissociation

TABLE II. Singlet triplet splittings, reaction energies for subsequent nitrile dissociation, TS (triplet to singlet) relaxations after nitrile release, and reaction energies for the subsequent water association [as sketched in Fig. 1(a)]. All values in (kcal/mol) as sketched in Fig. 1(a). PBE0/cc-pVTZ/SDD level of theory.

Compound	ST splitting[a]	Nitrile dissociation	TS relaxation	Water association
1	54.86 (47.46)	7.01	−18.09	−25.51
2	56.41 (47.46)	3.92	−17.41	−25.79
3	55.17 (46.03)	3.77	−17.62	−25.03
4	53.61 (44.89)	2.85	−16.24	−24.91
5	46.50 (46.03)	14.25	−17.76	−24.63
6	48.11 (43.17)	12.22	−14.38	−25.84
7	52.82 (41.74)	54.71	−13.36	−23.85
8	35.48 (37.45)	47.16	−10.02	−24.23
9	36.05 (38.88)	47.61	−9.81	−24.15
10	36.05 (39.17)	47.65	−9.85	−24.12
11	34.48 (37.17)	46.57	−9.83	−23.72
12	35.04 (38.03)	46.82	−10.08	−23.85
13	22.23	19.81	−7.87	−18.79
14	22.41	40.84	−8.20	−18.61
15	22.48	36.08	−9.12	−22.47

[a]Experimentally derived ST splittings from emission maxima taken from Ref. 28 in parenthesis.

occurs from the triplet states, the focus is on triplet BSO(Ru–NC) and BSO(Ru–L) values in the following.

Figure 8(a) shows the correlation between the Ru–NC bond strength and the quantum yield for water association, and Fig. 8(b) shows the corresponding correlation for the Ru–L bonds. In both cases, there is no significant correlation between these two quantities, Group 1 and Group 2 members (with the exception of outlier **12** from two clusters, as found for the correlation between ST splitting energies and QYs shown in Fig. 2).

The most striking result revealed by Fig. 8(a) is that Group 2 members **8**–**11** with the largest observed quantum yields for water association have the strongest Ru–NC bonds in their triplet state with BSO values between 0.883 and 0.888, which also contains the Ru–NC bond of the outlier **12**, whereas the members of Group 1, compounds **1**–**7**, with smaller QYs covering a large range of BSO values with compound **1** having the weakest Ru–NC bond (BSO = 0.847) and **7** the strongest Ru–NC bond (BSO = 0.894) of the whole set. Figure 8(b) shows a similar trend for the Ru–L bonds, i.e., Group 1 member BSOs are more spread out than those of Group 2 members. This leads to the important conclusion that modifying the Ru–NC and/or Ru–L bond strengths does not necessarily lead to a specific enhancement of the quantum yield, as clarified by the LMA analysis; modification of the quantum yield needs a more elaborate and complex effort.

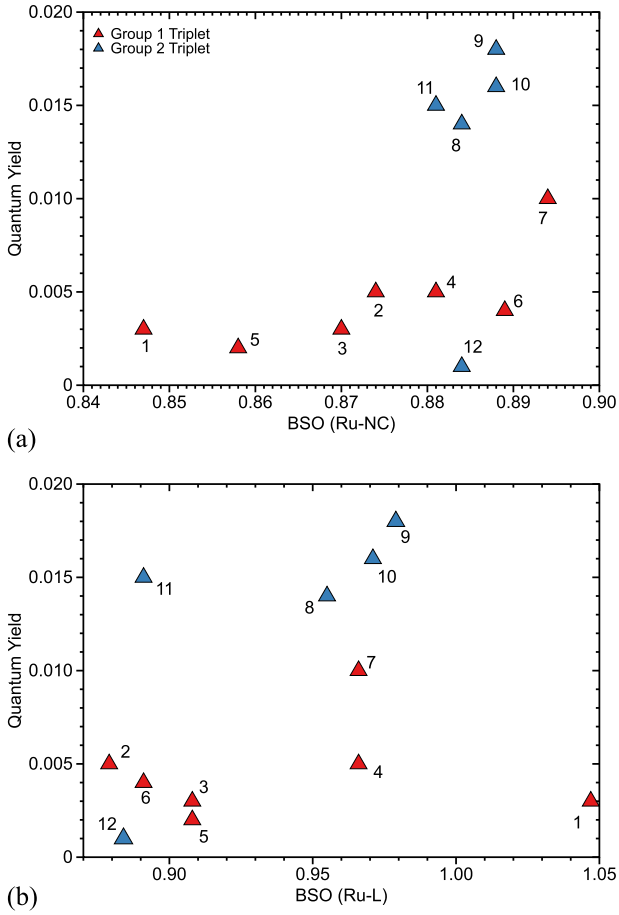

FIG. 8. Comparison of BSO values for the triplet states of compounds **1**–**12** (PBE0/cc-pVTZ/SDD level of theory) and experimental quantum yields taken from Ref. 28 (a) for R–NC bonds and (b) for Ru–L bonds.

C. Mechanism of nitrile release

Ongoing work is devoted to investigate the mechanism of the light induced ST transition, nitrile release, and water association with our Unified Reaction Valley Approach (URVA).[124] URVA analyzes the curvature of the reaction path traced out by the reacting species on the potential energy surface on their way from reactants via transition state to products. Curvature peaks mark important chemical events,[121,125] and the decomposition of the curvature peaks into internal coordinate components, such as bond length, bond angles, and puckering coordinates, elucidates which coordinates contribute to a certain chemical event such as bond forming/breaking or rehybridization.[126] In contrast, curvature minima reflect locations of minimal change, often denoting the transition from one chemical event to the next. The region between two curvature minima including a curvature peak identifies a reaction phase. In this way, different families of chemical reactions are characterized by different numbers and patterns of chemical phases, which can be used as their *fingerprint*.[124] Most important from an energetic point of view are the curvature peaks before the transition state because they identify the processes which contribute to the energy barrier.[121,124,125]

In the following, first results for the nitrile dissociation reaction for complex **1** as a representative for Group 1 and for complex **8** as a representative for Group 2 are highlighted. We used as reaction path the intrinsic reaction coordinate (IRC) path of Fukui[127] together with the improved reaction path following the procedure of Hratchian and Kraka.[128] The URVA analysis was performed with the program package pURVA.[129]

Figure 9 summarizes the results of the URVA analysis for complex **1**. Figure 9(a) shows the energy profile as a function of the reaction parameter *s*, Fig. 9(b) shows the scalar reaction path curvature and its decomposition into selected internal coordinate components, Fig. 9(c) illustrates changes in selected bond lengths, and Fig. 9(d) shows the changes of selected atomic NBO charges along the reaction path. The corresponding figure for complex **8** can be found in the supplementary material (Fig. S4). Reaction movies for both reactions illustrating the movement of all atoms at each point of the reaction path are also included in the supplementary material.

The reaction starts from the triplet complex with a Ru–NC bond length of 2.042 Å and ends at a van der Waals complex with a loosely connected nitrile ligand with an elongated Ru–NC bond of 2.754 Å [see Fig. 9(c)]. The activation and the reaction energies are 6.5 and 4.8 kcal/mol, respectively, i.e., dissociation proceeds with a small barrier and is a slightly endothermic process [see also Fig. 9(a)]. As revealed by the curvature profile [black solid line, Fig. 9(b)], there are six distinct reaction phases [marked with small blue numbers, Fig. 9(b)]. Before the transition state, there is one large curvature peak with a shoulder stretching into phase 3, which is responsible for the activation barrier. Most interesting to note is that this curvature peak results from bond, dihedral, and pyramidalization angles involving the metal and connected ligand atoms

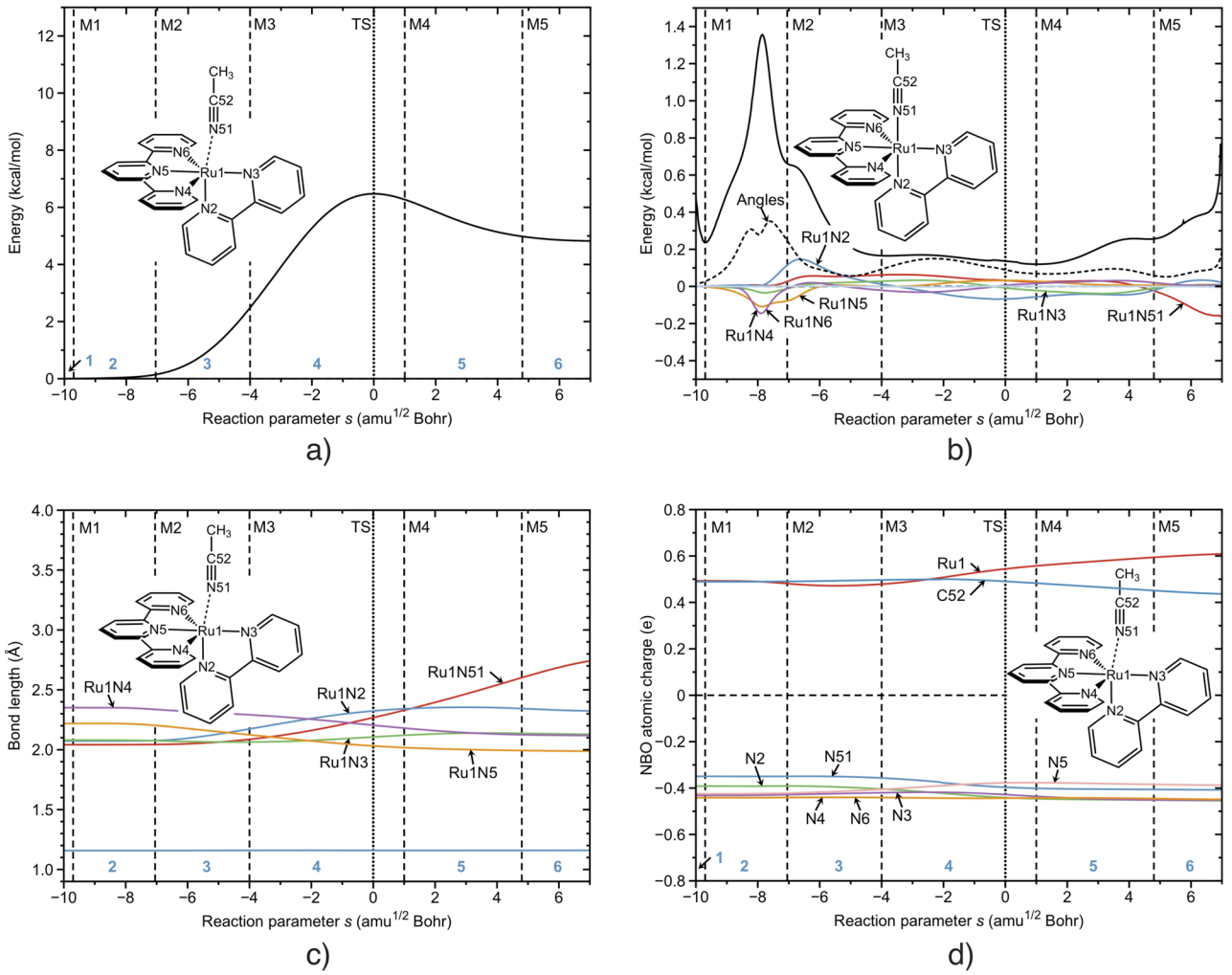

FIG. 9. URVA analysis for nitrile dissociation of complex **1**. (a) Energy profile. (b) Reaction path curvature and its decomposition into selected internal components. (c) Changes of the selected bond lengths. (d) Changes of the selected atomic charges. Curvature minima are shown as broken vertical lines and labeled as M1, M2, and so on. Reaction phases are indicated by blue numbers. The position of the transition state (TS) (s = 0) is indicated by a dotted line. Negative s values for the entrance and positive s values for the exit channel. PBE0/6-31g(d,p)/SDD level of theory.

[dashed black line, Fig. 9(b)], i.e., changes in the Ru coordination sphere in connection with reducing the coordination number from 6 to 5. In contrast, there is no significant curvature contribution from the Ru–NC component [red line in Fig. 9(b)] until phase 6, confirming the observation that there is no correlation between Ru–NC bond strength and ease of nitrile release. In the first three phases, the Ru–NC distance remains constant, starting in phase 4 the Ru–NC bond length linearly increases until reaching its final value at the end of phase 6. After TS, we observe a somewhat increasing polarization of the Ru–NC bond, making the Ru atom of this bond more positive, and the N atom of the Ru–NC bond slightly more negative [see Fig. 9(d)] contributing to the stabilization of the van der Waals complex. As illustrated in Fig. 10(b), nitrile release is driven by a change of the metal coordination sphere, which in turn supports the elongation/cleavage of the Ru–NC bond. This is often found in transition metal catalysis where changes of the metal sphere, which are less energy demanding than the direct bond breaking initiate a actual bond breaking step.[124,130,131] The same picture emerges for complex **8**. The reaction starts from the triplet complex with a Ru–NC bond length of 2.026 Å and ends at a van der Waals complex with a loosely connected nitrile ligand with an elongated Ru–NC bond of 2.819 Å [see Fig. S4(c) of the supplementary material]. The activation and the reaction energies are 6.9 and 6.6 kcal/mol, respectively [see Fig. S4(a) of the supplementary material], i.e., dissociation proceeds with a slightly larger barrier and somewhat increased endothermicity (1.6 kcal/mol) compared to complex **1**. The curvature pattern is somewhat different as revealed by the curvature profile [black solid line in Fig. S4(b)]. There are five distinct reaction phases [marked

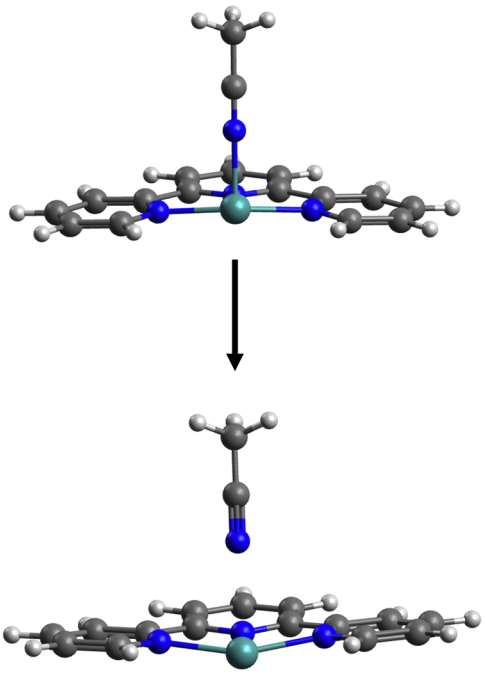

FIG. 10. Change of the Ru coordination sphere upon nitrile release for complex **1**. PBE0/cc-pVTZ/SDD level of theory.

with small blue numbers in Fig. S4(b) of the supplementary material]. The large curvature peak of the reaction profile of complex **1** is replaced by two smaller peaks, one in phase 2 and one in phase 4, with a small curvature enhancement in phase 3 in between. The final curvature peak at the end of phase 5 is more pronounced. However, as for complex **1**, the curvature peaks before the transition state are dominated by bond, dihedral, and pyramidalization angles involving the metal and connected ligand atoms [dashed black line in Fig. S4(b) of the supplementary material], i.e., again changes in the Ru coordination sphere in connection with reducing the coordination number from 6 to 5 drive the reaction. There is no significant curvature contribution from the Ru–NC component [red line in Fig. S4(b) of the supplementary material] until phase 5, confirming that there is no correlation between Ru–NC bond strength and ease of nitrile release for members of Group 1 with smaller QYs as well as for members of Group 2 with higher QYs. Also, for complex **8**, the Ru–NC distance remains constant in the first three phases, and in phase 4, the Ru–NC bond length starts to increase linearly until reaching its final value at the end of phase 5. The main difference between the two complexes can be seen in the larger polarization of the Ru–NC bond for complex **8**. At the end of the reaction, the Ru atom has a positive charge of 0.7 (compared to 0.6 for complex **1**) and the N atom of the Ru–NC bond has a negative charge of −3.8 [compared to −3.0 for complex **1**, see Fig. S4(d) of the supplementary material]. In summary, both reactions show a similar mechanism, which starts from the change of the metal coordination sphere initiating bond polarization due to electron density transfer between the Ru to N atoms and bond elongation. Therefore, we conclude that fine-tuning and new design efforts of nitrile releasing ruthenium compounds may benefit most from ancillary ligands L supporting the change of the ruthenium coordination sphere and enhancing the charge transfer between the Ru and the N atom of the nitrile group.

IV. CONCLUSIONS AND OUTLOOK

The main goals of this study were (i) to calculate local bond properties for a set nitrile releasing ruthenium(II) complexes with various bidentate ancillary ligand L, particularly Ru–NC and Ru–L bond strengths utilizing local mode force constants complemented with QTAIM and NBO analyses; (ii) to explore how these local properties relate to one another and how they are connected to global properties, i.e., QYs for ligand exchange and ST splitting energies, introduced by Loftus *et al.*[28] as a measure of nitrile release efficiency; and (iii) to propose new ancillary ligands and assess their value for further experimental exploration. The most important outcomes of this study can be summarized as follows:

- Compounds with the highest quantum yields have the strongest Ru–NC bonds suggesting that breaking the Ru–NC bond is not the driving force for the delivery process rather than the change of the metal framework, as revealed by first results of a unified reaction valley approach investigation of the mechanism.
- Compounds with the highest quantum yields show larger electronic structure changes upon singlet–triplet excitation, i.e., larger changes in bond strength, covalency, and difference between singlet and the triplet HOMOs, with exception of compound **12**, identified as an outlier. Thus, potential candidates should follow this trend as well.
- Our new compounds **13**–**15** show the same triplet HOMO/LUMO electron density redistribution as the most successful compounds synthesized by Loftus *et al.*,[28] and even smaller ST splitting energies and Ru-d orbital contributions than the original Loftus set, qualifying them as valuable candidates to be explored by experiment.

In summary, this work provides new insights into the interplay of local properties and experimental quantum yields forming in synergy a powerful tool for fine tuning of existing and future design of new nitrile releasing ruthenium compounds. We hope that this work will bring theoretical and experimental studies closer together and serves as an incubator for future collaboration between computational chemists and their experimental colleagues.

SUPPLEMENTARY MATERIAL

The supplementary material contains the following: experimental vs calculated frequencies for Ru–NC bonds, bond strength order differences between singlet and triplet states for Ru–NC and Ru–L bonds, additional bond lengths comparison for Ru–NC and Ru–L bonds, URVA analysis for complex **8**, HOMO and LUMO orbital plots for compounds **1**–**15** in their singlet and triplet states, Cartesian coordinates of all original 15 ruthenium complexes (singlet and triplet states, geometry optimized at the PBE0/cc-pVTZ/SDD level of theory), Cartesian coordinates of all 15 ruthenium complexes after nitrile dissociation (singlet and triplet states, geometry optimized at the PBE0/cc-pVTZ/SDD level

of theory), and Cartesian coordinates of all 15 ruthenium–H_2O complexes (singlet states, geometry optimized at the PBE0/cc-pVTZ/SDD level of theory). Reaction movies for the nitrile release of complexes **1** and **8**.

ACKNOWLEDGMENTS

We thank SMU for providing generous computational resources and the Moody School for providing a University fellowship. This work was financially supported by the National Science Foundation (Grant No. CHE 2102461) and the DSF Charitable Foundation.

AUTHOR DECLARATIONS

Conflict of Interest

The authors have no conflicts to disclose.

Author Contributions

Margaret McCutcheon: Data curation (equal); Formal analysis (equal); Validation (equal); Visualization (equal). **Marek Freindorf:** Data curation (equal); Formal analysis (equal); Investigation (equal); Validation (equal); Visualization (equal). **Elfi Kraka:** Conceptualization (lead); Formal analysis (equal); Funding acquisition (lead); Investigation (equal); Methodology (equal); Project administration (lead); Resources (equal); Supervision (lead); Validation (equal); Writing – original draft (lead); Writing – review and editing (lead).

DATA AVAILABILITY

The data that support the findings of this study are available within the article and its supplementary material.

REFERENCES

[1]S. Silvestri, I. Cirilli, F. Marcheggiani, P. Dludla, G. Lupidi, R. Pettinari, F. Marchetti, C. Di Nicola, G. Falcioni, C. Marchini, P. Orlando, L. Tiano, and A. Amici, "Evaluation of anticancer role of a novel ruthenium(II)-based compound compared with NAMI-A and cisplatin in impairing mitochondrial functionality and promoting oxidative stress in triple negative breast cancer models," Mitochondrion **56**, 25–34 (2021).

[2]J. Coverdale, T. Laroiya-McCarron, and I. Romero-Canelón, "Designing ruthenium anticancer drugs: What have we learnt from the key drug candidates?," Inorganics **7**, 31 (2019).

[3]A. Busemann, I. Flaspohler, X.-Q. Zhou, C. Schmidt, S. K. Goetzfried, V. H. S. van Rixel, I. Ott, M. A. Siegler, and S. Bonnet, "Ruthenium-based PACT agents based on bisquinoline chelates: Synthesis, photochemistry, and cytotoxicity," JBIC, J. Biol. Inorg. Chem. **26**, 667–674 (2021).

[4]S. Thota, D. A. Rodrigues, D. C. Crans, and E. J. Barreiro, "Ru(II) compounds: Next-generation anticancer metallotherapeutics?," J. Med. Chem. **61**, 5805–5821 (2018).

[5]O. A. Lenis-Rojas, M. P. Robalo, A. I. Tomaz, A. R. Fernandes, C. Roma-Rodrigues, R. G. Teixeira, F. Marques, M. Folgueira, J. Yáñez, A. A. Gonzalez, M. Salamini-Montemurri, D. Pech-Puch, D. Vázquez-García, M. L. Torres, A. Fernández, and J. J. Fernández, "Half-sandwich Ru(*p*-cymene) compounds with diphosphanes: *In vitro* and *in vivo* evaluation as potential anticancer metallodrugs," Inorg. Chem. **60**, 2914–2930 (2021).

[6]J. Haribabu, S. Srividya, R. Umapathi, D. Gayathri, P. Venkatesu, N. Bhuvanesh, and R. Karvembu, "Enhanced anticancer activity of half-sandwich Ru(II)-*p*-cymene complex bearing heterocyclic hydrazone ligand," Inorg. Chem. Commun. **119**, 108054 (2020).

[7]O. A. Lenis-Rojas, R. Cabral, B. Carvalho, S. Friães, C. Roma-Rodrigues, J. A. A. Fernández, S. F. Vila, L. Sanchez, C. S. B. Gomes, A. R. Fernandes, and B. Royo, "Triazole-based half-sandwich ruthenium(II) compounds: From *in vitro* antiproliferative potential to *in vivo* toxicity evaluation," Inorg. Chem. **60**, 8011–8026 (2021).

[8]H. Geisler, J. Westermayr, K. Cseh, D. Wenisch, V. Fuchs, S. Harringer, S. Plutzar, N. Gajic, M. Hejl, M. A. Jakupec, P. Marquetand, and W. Kandioller, "Tridentate 3-substituted naphthoquinone ruthenium arene complexes: Synthesis, characterization, aqueous behavior, and theoretical and biological studies," Inorg. Chem. **60**, 9805–9819 (2021).

[9]T. Han, Y. Wu, W. Han, K. Yan, J. Zhao, and Y. Sun, "Antitumor effect of organometallic half-sandwich Ru(II)–arene complexes bearing a glutathione *S*-transferase inhibitor," Inorg. Chem. **60**, 13051–13061 (2021).

[10]J. Grau, V. Noe, C. Ciudad, M. J. Prieto, M. Font-Bardia, T. Calvet, and V. Moreno, "New π-arene ruthenium(II) piano-stool complexes with nitrogen ligands," J. Inorg. Biochem. **109**, 72–81 (2012).

[11]A. A. Nazarov, C. G. Hartinger, and P. J. Dyson, "Opening the lid on piano-stool complexes: An account of ruthenium(II)–arene complexes with medicinal applications," J. Organomet. Chem. **751**, 251–260 (2014).

[12]L. Rafols, D. Josa, D. Aguilà, L. A. Barrios, O. Roubeau, J. Cirera, V. Soto-Cerrato, R. Pérez-Tomás, M. Martínez, A. Grabulosa, and P. Gamez, "Piano-stool ruthenium(II) complexes with delayed cytotoxic activity: Origin of the lag time," Inorg. Chem. **60**, 7974–7990 (2021).

[13]M. M. da Silva, G. H. Ribeiro, M. S. de Camargo, A. G. Ferreira, L. Ribeiro, M. I. F. Barbosa, V. M. Deflon, S. Castelli, A. Desideri, R. S. Corrêa, A. B. Ribeiro, H. D. Nicolella, S. D. Ozelin, D. C. Tavares, and A. A. Batista, "Ruthenium(II) diphosphine complexes with mercapto ligands that inhibit topoisomerase IB and suppress tumor growth in vivo," Inorg. Chem. **60**, 14174–14189 (2021).

[14]S. Gupta, J. M. Vandevord, L. M. Loftus, N. Toupin, M. H. Al-Afyouni, T. N. Rohrabaugh, C. Turro, and J. J. Kodanko, "Ru(II)-based acetylacetonate complexes induce apoptosis selectively in cancer cells," Inorg. Chem. **60**, 18964–18974 (2021).

[15]M. Klajner, C. Licona, L. Fetzer, P. Hebraud, G. Mellitzer, M. Pfeffer, S. Harlepp, and C. Gaiddon, "Subcellular localization and transport kinetics of ruthenium organometallic anticancer compounds in living cells: A dose-dependent role for amino acid and iron transporters," Inorg. Chem. **53**, 5150–5158 (2014).

[16]S. Y. Lee, C. Y. Kim, and T.-G. Nam, "Ruthenium complexes as anticancer agents: A brief history and perspectives," Drug Des., Dev. Ther. **14**, 5375–5392 (2020).

[17]E. S. Antonarakis and A. Emadi, "Ruthenium-based chemotherapeutics: Are they ready for prime time?," Cancer Chemother. Pharmacol. **66**, 1–9 (2010).

[18]S. Paul, P. Kundu, P. Kondaiah, and A. R. Chakravarty, "BODIPY-ruthenium(II) bis-terpyridine complexes for cellular imaging and type-I/-II photodynamic therapy," Inorg. Chem. **60**, 16178–16193 (2021).

[19]G. Han, G. Li, J. Huang, C. Han, C. Turro, and Y. Sun, "Two-photon-absorbing ruthenium complexes enable near infrared light-driven photocatalysis," Nat. Commun. **13**, 2288-1–2288-13 (2022).

[20]J. Pan, L. Jiang, C.-F. Chan, T.-H. Tsoi, K.-K. Shiu, D. W. J. Kwong, W.-T. Wong, W.-K. Wong, and K.-L. Wong, "Excitation energy transfer in ruthenium (II)-porphyrin conjugates led to enhanced emission quantum yield and $^1O_2$ generation," J. Lumin. **184**, 89–95 (2017).

[21]A. Jain, N. T. Garrett, and Z. P. Malone, "Ruthenium-based photoactive metalloantibiotics," Photochem. Photobiol. **98**, 6–16 (2022).

[22]A. P. de Sousa, A. C. S. Gondim, E. H. S. Sousa, M. A. de Vasconcelos, E. H. Teixeira, B. P. Bezerra, A. P. Ayala, P. H. R. Martins, L. G. de França Lopes, and A. K. M. Holanda, "An unusual bidentate methionine ruthenium(II) complex: Photo-uncaging and antimicrobial activity," JBIC, J. Biol. Inorg. Chem. **25**, 419–428 (2020).

[23]J. Liu, W. Kang, and W. Wang, "Photocleavage-based photoresponsive drug delivery," Photochem. Photobiol. **98**, 288–302 (2022).

[24]A. Awada, F. Loiseau, and D. Jouvenot, "Light-induced ejection of a tridentate ligand from a ruthenium(II) complex," Eur. J. Inorg. Chem. **2021**, 4539–4542.

[25]S. J. Steinke, S. Gupta, E. J. Piechota, C. E. Moore, J. J. Kodanko, and C. Turro, "Photocytotoxicity and photoinduced phosphine ligand exchange in a Ru(II) polypyridyl complex," Chem. Sci. **13**, 1933–1945 (2022).

[26]A. P. Lanquist, S. Gupta, K. F. Al-Afyouni, M. Al-Afyouni, J. J. Kodanko, and C. Turro, "Trifluoromethyl substitution enhances photoinduced activity against breast cancer cells but reduces ligand exchange in Ru(II) complex," Chem. Sci. **12**, 12056–12067 (2021).
[27]P. Thangavel, B. Viswanath, and S. Kim, "Recent developments in the nanostructured materials functionalized with ruthenium complexes for targeted drug delivery to tumors," Int. J. Nanomed. **12**, 2749–2758 (2017).
[28]L. M. Loftus, K. F. Al-Afyouni, T. N. Rohrabaugh, J. C. Gallucci, C. E. Moore, J. J. Rack, and C. Turro, "Unexpected role of Ru(II) orbital and spin contribution on photoinduced ligand exchange: New mechanism to access the photodynamic therapy window," J. Phys. Chem. C **123**, 10291–10299 (2019).
[29]J. D. Knoll and C. Turro, "Control and utilization of ruthenium and rhodium metal complex excited states for photoactivated cancer therapy," Coord. Chem. Rev. **282-283**, 110–126 (2015).
[30]Z. Dai and Z. Wang, "Photoactivatable platinum-based anticancer drugs: Mode of photoactivation and mechanism of action," Molecules **25**, 5167 (2020).
[31]B. S. McGhie and J. R. Aldrich-Wright, "Photoactive and luminescent transition metal complexes as anticancer agents: A guiding light in the search for new and improved cancer treatments," Biomedicines **10**, 578 (2022).
[32]R. Paprocka, M. Wiese-Szadkowska, S. Janciauskiene, T. Kosmalski, M. Kulik, and A. Helmin-Basa, "Latest developments in metal complexes as anticancer agents," Coord. Chem. Rev. **452**, 214307 (2022).
[33]M. Muddassir, A. Alarifi, and M. Afzal, "A new piano-stool ruthenium(II) *p*-cymene-based complex: Crystallographic, Hirshfeld surface, DFT, and luminescent studies," Crystals **11**, 13 (2020).
[34]O. S. Wenger, "Is iron the new ruthenium?," Eur. J. Chem. **25**, 6043–6052 (2019).
[35]L. Schmid, C. Kerzig, A. Prescimone, and O. S. Wenger, "Photostable ruthenium(II) isocyanoborato luminophores and their use in energy transfer and photoredox catalysis," JACS Au **1**, 819–832 (2021).
[36]S. I. Gorelsky, E. S. Dodsworth, A. B. P. Lever, and A. A. Vlcek, "Trends in metal–ligand orbital mixing in generic series of ruthenium N-donor ligand complexes—Effect on electronic spectra and redox properties," Coord. Chem. Rev. **174**, 469–494 (1998).
[37]M. Abrahamsson, H. Wolpher, O. Johansson, J. Larsson, M. Kritikos, L. Eriksson, P.-O. Norrby, J. Bergquist, L. Sun, B. Åkermark, and L. Hammarström, "A new strategy for the improvement of photophysical properties in ruthenium(II) polypyridyl complexes. Synthesis and photophysical and electrochemical characterization of six mononuclear ruthenium(II) bisterpyridine-type complexes," Inorg. Chem. **44**, 3215–3225 (2005).
[38]P. S. Wagenknecht and P. C. Ford, "Metal centered ligand field excited states: Their roles in the design and performance of transition metal based photochemical molecular devices," Coord. Chem. Rev. **255**, 591–616 (2011).
[39]G. Leem, Z. A. Morseth, K. R. Wee, J. Jiang, M. K. Brennaman, J. M. Papanikolas, and K. S. Schanze, "Polymer-based ruthenium(II) polypyridyl chromophores on TiO_2 for solar energy conversion," Asian J. Chem. **11**, 1257–1267 (2016).
[40]P. Spence, J. Fielden, and Z. A. E. Waller, "Beyond solvent exclusion: i-Motif detecting capability and an alternative DNA light-switching mechanism in a ruthenium(II) polypyridyl complex," J. Am. Chem. Soc. **142**, 13856–13866 (2020).
[41]L.-N. Ji, X.-H. Zou, and J.-G. Liu, "Shape- and enantioselective interaction of Ru(II)/Co(III) polypyridyl complexes with DNA," Coord. Chem. Rev. **216-217**, 513–536 (2001).
[42]B. W.-K. Chu and V. W.-W. Yam, "Sensitive single-layered oxygen-sensing systems: Polypyridyl ruthenium(II) complexes covalently attached or deposited as Langmuir–Blodgett monolayer on glass surfaces," Langmuir **22**, 7437–7443 (2006).
[43]S. Kumar, S. Singh, A. Kumar, and P. Kumar, "Recognition, mechanistic investigation and applications for the detection of biorelevant $Cu^{2+}/Fe^{2+}/Fe^{3+}$ ions by ruthenium(II)-polypyridyl based fluorescent sensors," Dalton Trans. **50**, 2705–2721 (2021).
[44]R. Naumann and M. Goez, "How the sustainable solvent water unleashes the photoredox catalytic potential of ruthenium polypyridyl complexes for pinacol couplings," Green Chem. **21**, 4470–4474 (2019).
[45]X. Wang, Y. Wang, X. Li, Z. Yu, C. Song, and Y. Du, "Nitrile-containing pharmaceuticals: Target, mechanism of action, and their SAR studies," RSC Med. Chem. **12**, 1650–1671 (2021).
[46]H. Wang, N. J. DeYonker, X. Zhang, C. Zhao, L. Ji, and Z.-W. Mao, "Photodissociation of a ruthenium(II) arene complex and its subsequent interactions with biomolecules: A density functional theory study," J. Mol. Model. **18**, 4675–4686 (2012).
[47]J. Karges, R. W. Stokes, and S. M. Cohen, "Photorelease of a metal-binding pharmacophore from a Ru(II) polypyridine complex," Dalton Trans. **50**, 2757–2765 (2021).
[48]F. Barragán, P. López-Senín, L. Salassa, S. Betanzos-Lara, A. Habtemariam, V. Moreno, P. J. Sadler, and V. Marchán, "Photocontrolled DNA binding of a receptor-targeted organometallic ruthenium(II) complex," J. Am. Chem. Soc. **133**, 14098–14108 (2011).
[49]S. Betanzos-Lara, L. Salassa, A. Habtemariam, and P. J. Sadler, "Photocontrolled nucleobase binding to an organometallic Ru^{II} arene complex," Chem. Commun. **43**, 6622 (2009).
[50]L. M. Loftus, J. J. Rack, and C. Turro, "Photoinduced ligand dissociation follows reverse energy gap law: Nitrile photodissociation from low energy ^{3}MLCT excited states," Chem. Commun. **56**, 4070–4073 (2020).
[51]L. M. Loftus, A. Li, K. L. Fillman, P. D. Martin, J. J. Kodanko, and C. Turro, "Unusual role of excited state mixing in the enhancement of photoinduced ligand exchange in Ru(II) complexes," J. Am. Chem. Soc. **139**, 18295–18306 (2017).
[52]A. Cotic, I. Ramirez-Wierzbickia, G. E. Pieslingera, and B. M. A. andAlejandro Cadranela, "Ligand field states dominate excited state decay in *trans*-$[Ru(py)_4Cl_2]$ MLCT chromophores," Inorg. Chim. Acta **518**, 120246-1–120246-8 (2021).
[53]G. Lemercier, A. Bonne, M. Four, and L. M. Lawson-Daku, "^{3}MLCT excited states in Ru(II) complexes: Reactivity and related two-photon absorption applications in the near-infrared spectral range," C. R. Chim. **11**, 709–715 (2008).
[54]E. Kraka, W. Zou, and Y. Tao, "Decoding chemical information from vibrational spectroscopy data: Local vibrational mode theory," Wiley Interdiscip. Rev.: Comput. Mol. Sci. **10**, 1480 (2020).
[55]R. F. W. Bader, *Atoms in Molecules: A Quantum Theory*, International Series of Monographs on Chemistry (Clarendon Press, 1994).
[56]R. F. W. Bader, "A quantum theory of molecular structure and its applications," Chem. Rev. **91**, 893–928 (1991).
[57]R. F. W. Bader, "The quantum mechanical basis of conceptual chemistry," Monatsh. Chem. **136**, 819–854 (2005).
[58]P. L. Popelier, *Atoms in Molecules: An Introduction* (Prentice Hall, 2000).
[59]A. E. Reed, L. A. Curtiss, and F. Weinhold, "Intermolecular interactions from a natural bond orbital, donor-acceptor viewpoint," Chem. Rev. **88**, 899–926 (1988).
[60]F. Weinhold and C. R. Landis, *Valency and Bonding: A Natural Bond Orbital Donor–Acceptor Perspective* (Cambridge University Press, 2003).
[61]J. Chen, J. Wang, Y. Deng, T. Wang, T. Miao, C. Li, X. Cai, Y. Liu, J. Henri, and L. Chen, "Ru(II) complexes bearing O, O-chelated ligands induced apoptosis in A549 cells through the mitochondrial apoptotic pathway," Bioinorg. Chem. Appl. **2020**, 8890950-1–8890950-16.
[62]G. K. Mutua, R. Bellam, D. Jaganyi, and A. Mambanda, "The role of *N*,*N*-chelate ligand on the reactivity of (η^6-*p*-cymene)Ru(II) complexes: Kinetics, DNA and protein interaction studies," J. Coord. Chem. **72**, 2931–2956 (2019).
[63]Z. Konkoli and D. Cremer, "A new way of analyzing vibrational spectra. I. Derivation of adiabatic internal modes," Int. J. Quantum Chem. **67**, 1–9 (1998).
[64]Z. Konkoli, J. A. Larsson, and D. Cremer, "A new way of analyzing vibrational spectra. II. Comparison of internal mode frequencies," Int. J. Quantum Chem. **67**, 11–27 (1998).
[65]Z. Konkoli and D. Cremer, "A new way of analyzing vibrational spectra. III. Characterization of normal vibrational modes in terms of internal vibrational modes," Int. J. Quantum Chem. **67**, 29–40 (1998).
[66]Z. Konkoli, J. A. Larsson, and D. Cremer, "A new way of analyzing vibrational spectra. IV. Application and testing of adiabatic modes within the concept of the characterization of normal modes," Int. J. Quantum Chem. **67**, 41–55 (1998).
[67]D. Cremer, J. A. Larsson, and E. Kraka, "New developments in the analysis of vibrational spectra on the use of adiabatic internal vibrational modes," Theor. Comput. Chem. **5**, 259–327 (1998).
[68]E. B. Wilson, J. C. Decius, and P. C. M. Cross, *Molecular Vibrations: The Theory of Infrared and Raman Vibrational Spectra* (McGraw-Hill, New York, 1955), pp. 59–136.

[69]W. Zou and D. Cremer, "C_2 in a box: Determining its intrinsic bond strength for the $X^1\ \Sigma_g^+$ ground state," Chem. - Eur. J. **22**, 4087–4097 (2016).
[70]A. A. A. Delgado, A. Humason, R. Kalescky, M. Freindorf, and E. Kraka, "Exceptionally long covalent CC bonds—A local vibrational mode study," Molecules **26**, 950-1–950-25 (2021).
[71]E. Kraka, J. A. Larsson, and D. Cremer, "Generalization of the Badger rule based on the use of adiabatic vibrational modes," in *Computational Spectroscopy*, edited by J. Grunenberg (Wiley, New York, 2010), pp. 105–149.
[72]R. Kalescky, E. Kraka, and D. Cremer, "Identification of the strongest bonds in chemistry," J. Phys. Chem. A **117**, 8981–8995 (2013).
[73]E. Kraka and D. Cremer, "Characterization of CF bonds with multiple-bond character: Bond lengths, stretching force constants, and bond dissociation energies," ChemPhysChem **10**, 686–698 (2009).
[74]E. Kraka, D. Setiawan, and D. Cremer, "Re-evaluation of the bond length–bond strength rule: The stronger bond is not always the shorter bond," J. Comput. Chem. **37**, 130–142 (2015).
[75]D. Setiawan, D. Sethio, D. Cremer, and E. Kraka, "From strong to weak NF bonds: On the design of a new class of fluorinating agents," Phys. Chem. Chem. Phys. **20**, 23913–23927 (2018).
[76]M. Freindorf, S. Yannacone, V. Oliveira, N. Verma, and E. Kraka, "Halogen bonding involving I_2 and d^8 transition-metal pincer complexes," Crystals **11**, 373-1–373-21 (2021).
[77]V. Oliveira, E. Kraka, and D. Cremer, "The intrinsic strength of the halogen bond: Electrostatic and covalent contributions described by coupled cluster theory," Phys. Chem. Chem. Phys. **18**, 33031–33046 (2016).
[78]V. Oliveira, E. Kraka, and D. Cremer, "Quantitative assessment of halogen bonding utilizing vibrational spectroscopy," Inorg. Chem. **56**, 488–502 (2016).
[79]V. Oliveira and D. Cremer, "Transition from metal-ligand bonding to halogen bonding involving a metal as halogen acceptor: A study of Cu, Ag, Au, Pt, and Hg complexes," Chem. Phys. Lett. **681**, 56–63 (2017).
[80]S. Yannacone, V. Oliveira, N. Verma, and E. Kraka, "A continuum from halogen bonds to covalent bonds: Where do λ^3 iodanes fit?," Inorganics **7**, 47 (2019).
[81]V. P. Oliveira, B. L. Marcial, F. B. C. Machado, and E. Kraka, "Metal–halogen bonding seen through the eyes of vibrational spectroscopy," Materials **13**, 55 (2020).
[82]V. Oliveira, D. Cremer, and E. Kraka, "The many facets of chalcogen bonding: Described by vibrational spectroscopy," J. Phys. Chem. A **121**, 6845–6862 (2017).
[83]V. Oliveira and E. Kraka, "Systematic coupled cluster study of noncovalent interactions involving halogens, chalcogens, and pnicogens," J. Phys. Chem. A **121**, 9544–9556 (2017).
[84]D. Setiawan, E. Kraka, and D. Cremer, "Hidden bond anomalies: The peculiar case of the fluorinated amine chalcogenides," J. Phys. Chem. A **119**, 9541–9556 (2015).
[85]D. Setiawan, E. Kraka, and D. Cremer, "Strength of the pnicogen bond in complexes involving group Va elements N, P, and As," J. Phys. Chem. A **119**, 1642–1656 (2014).
[86]D. Setiawan, E. Kraka, and D. Cremer, "Description of pnicogen bonding with the help of vibrational spectroscopy—The missing link between theory and experiment," Chem. Phys. Lett. **614**, 136–142 (2014).
[87]D. Setiawan and D. Cremer, "Super-pnicogen bonding in the radical anion of the fluorophosphine dimer," Chem. Phys. Lett. **662**, 182–187 (2016).
[88]D. Sethio, V. Oliveira, and E. Kraka, "Quantitative assessment of tetrel bonding utilizing vibrational spectroscopy," Molecules **23**, 2763-1–2763-21 (2018).
[89]M. Freindorf, E. Kraka, and D. Cremer, "A comprehensive analysis of hydrogen bond interactions based on local vibrational modes," Int. J. Quantum Chem. **112**, 3174–3187 (2012).
[90]R. Kalescky, W. Zou, E. Kraka, and D. Cremer, "Local vibrational modes of the water dimer—Comparison of theory and experiment," Chem. Phys. Lett. **554**, 243–247 (2012).
[91]R. Kalescky, E. Kraka, and D. Cremer, "Local vibrational modes of the formic acid dimer—The strength of the double hydrogen bond," Mol. Phys. **111**, 1497–1510 (2013).
[92]Y. Tao, W. Zou, J. Jia, W. Li, and D. Cremer, "Different ways of hydrogen bonding in water—Why does warm water freeze faster than cold water?," J. Chem. Theory Comput. **13**, 55–76 (2017).
[93]Y. Tao, W. Zou, and E. Kraka, "Strengthening of hydrogen bonding with the push-pull effect," Chem. Phys. Lett. **685**, 251–258 (2017).
[94]M. Z. Makoś, M. Freindorf, D. Sethio, and E. Kraka, "New insights into Fe–H_2 and Fe–H^- bonding of a [NiFe] hydrogenase mimic: A local vibrational mode study," Theor. Chem. Acc. **138**, 76 (2019).
[95]S. Lyu, N. Beiranvand, M. Freindorf, and E. Kraka, "Interplay of ring puckering and hydrogen bonding in deoxyribonucleosides," J. Phys. Chem. A **123**, 7087–7103 (2019).
[96]N. Verma, Y. Tao, and E. Kraka, "Systematic detection and characterization of hydrogen bonding in proteins via local vibrational modes," J. Phys. Chem. B **125**, 2551–2565 (2021).
[97]N. Beiranvand, M. Freindorf, and E. Kraka, "Hydrogen bonding in natural and unnatural base pairs—A local vibrational mode study," Molecules **26**, 2268-1–2268-22 (2021).
[98]S. Yannacone, M. Freindorf, Y. Tao, W. Zou, and E. Kraka, "Local vibrational mode analysis of π–hole interactions between aryl donors and small molecule acceptors," Crystals **10**, 556-1–556-25 (2020).
[99]D. Cremer and E. Kraka, "Chemical bonds without bonding electron density—Does the difference electron-density analysis suffice for a description of the chemical bond?," Angew. Chem., Int. Ed. **23**, 627–628 (1984).
[100]D. Cremer and E. Kraka, "A description of the chemical bond in terms of local properties of electron density and energy," Croat. Chem. Acta **57**, 1259–1281 (1984).
[101]F. Weinhold, "The path to natural bond orbitals," Isr. J. Chem. **62**, e202100026 (2021).
[102]W. Kohn, A. D. Becke, and R. G. Parr, "Density functional theory of electronic structure," J. Phys. Chem. **100**, 12974–12980 (1996).
[103]W. Kohn, A. D. Becke, and R. G. Parr, "Perspective: Fifty years of density-functional theory in chemical physics," J. Chem. Phys. **140**, 18A301-1–18A301-18 (2014).
[104]W. Koch and M. C. Holthausen, *A Chemist's Guide to Density Functional Theory*, 2nd ed. (Wiley-VCH Verlag GmbH, 2001).
[105]N. Mardirossian and M. Head-Gordon, "Thirty years of density functional theory in computational chemistry: An overview and extensive assessment of 200 density functionals," Mol. Phys. **115**, 2315–2372 (2017).
[106]C. Adamo and V. Barone, "Toward reliable density functional methods without adjustable parameters: The PBE0 model," J. Chem. Phys. **110**, 6158–6170 (1999).
[107]M. Niskanen, P. Hirva, and M. Haukka, "Computational DFT study of ruthenium tetracarbonyl polymer," J. Chem. Theory Comput. **5**, 1084–1090 (2009).
[108]G.-d. Li, L.-m. Chen, X.-y. Wang, L.-f. Wu, X.-m. Jie, and J.-c. Chen, "Electronic structures, DNA-binding, SAR, and spectral properties of ruthenium methylimidazole complexes $[Ru(MeIm)_4L]^{2+}$ (L=iip, tip, 2ntz)," Chin. J. Chem. Phys. **27**, 159–167 (2014).
[109]R. A. Kendall, T. H. Dunning, and R. J. Harrison, "Electron affinities of the first-row atoms revisited. Systematic basis sets and wave functions," J. Chem. Phys. **96**, 6796–6806 (1992).
[110]D. Andrae, U. Häußermann, M. Dolg, H. Stoll, and H. Preuß, "Energy-adjusted *ab initio* pseudopotentials for the second and third row transition elements," Theor. Chim. Acta **77**, 123–141 (1990).
[111]J. B. Goodenough, "Spin-orbit-coupling effects in transition-metal compounds," Phys. Rev. Lett. **171**, 466–479 (1968).
[112]B. P. Pritchard, D. Altarawy, B. Didier, T. D. Gibson, and T. L. Windus, "New basis set exchange: An open, up-to-date resource for the molecular sciences community," J. Chem. Inf. Model. **59**, 4814–4820 (2019).
[113]X. Xu and D. G. Truhlar, "Accuracy of effective core potentials and basis sets for density functional calculations, including relativistic effects, as illustrated by calculations on arsenic compounds," J. Chem. Theory Comput. **7**, 2766–2779 (2011).
[114]A. Garza-Ortiz, P. Uma Maheswari, M. Siegler, A. L. Spek, and J. Reedijk, "A new family of Ru(II) complexes with a tridentate pyridine Schiff-base ligand and bidentate co-ligands: Synthesis, characterization, structure and *in vitro* cytotoxicity studies," New J. Chem. **37**, 3450 (2013).
[115]Z. Rinkevicius, L. Telyatnyk, O. Vahtras, and H. Ågren, "Density functional theory for hyperfine coupling constants with the restricted-unrestricted approach," J. Chem. Phys. **121**, 7614 (2004).

[116]J. Gräfenstein, D. Izotov, and D. Cremer, "Avoiding singularity problems associated with meta-GGA (generalized gradient approximation) exchange and correlation functionals containing the kinetic energy density," J. Chem. Phys. **127**, 214103 (2007).
[117]M. J. Frisch, G. W. Trucks, H. B. Schlegel, G. E. Scuseria, M. A. Robb, J. R. Cheeseman, G. Scalmani, V. Barone, G. A. Petersson, H. Nakatsuji, X. Li, M. Caricato, A. V. Marenich, J. Bloino, B. G. Janesko, R. Gomperts, B. Mennucci, H. P. Hratchian, J. V. Ortiz, A. F. Izmaylov, J. L. Sonnenberg, D. Williams-Young, F. Ding, F. Lipparini, F. Egidi, J. Goings, B. Peng, A. Petrone, T. Henderson, D. Ranasinghe, V. G. Zakrzewski, J. Gao, N. Rega, G. Zheng, W. Liang, M. Hada, M. Ehara, K. Toyota, R. Fukuda, J. Hasegawa, M. Ishida, T. Nakajima, Y. Honda, O. Kitao, H. Nakai, T. Vreven, K. Throssell, J. A. Montgomery, Jr., J. E. Peralta, F. Ogliaro, M. J. Bearpark, J. J. Heyd, E. N. Brothers, K. N. Kudin, V. N. Staroverov, T. A. Keith, R. Kobayashi, J. Normand, K. Raghavachari, A. P. Rendell, J. C. Burant, S. S. Iyengar, J. Tomasi, M. Cossi, J. M. Millam, M. Klene, C. Adamo, R. Cammi, J. W. Ochterski, R. L. Martin, K. Morokuma, O. Farkas, J. B. Foresman, and D. J. Fox, Gaussian 16 Revision A.03, Gaussian, Inc., Wallingford, CT, 2016.
[118]W. Zou, Y. Tao, M. Freindorf, M. Makos, N. Verma, and E. Kraka, "LModeA," (2020).
[119]T. A. Keith, AIMAll Version 17.11.14, K. Gristmill Software, Overland Park, KS, 2017, aim.tkgristmill.com.
[120]E. D. Glendening, C. R. Landis, and F. Weinhold, "NBO 6.0: Natural bond orbital analysis program," J. Comput. Chem. **34**, 1429–1437 (2013).
[121]D. Cremer and E. Kraka, "From molecular vibrations to bonding, chemical reactions, and reaction mechanism," Curr. Org. Chem. **14**, 1524–1560 (2010).
[122]R. Kalescky, E. Kraka, and D. Cremer, "Are carbon–halogen double and triple bonds possible?," Int. J. Quantum Chem. **114**, 1060–1072 (2014).
[123]R. Kalescky, W. Zou, E. Kraka, and D. Cremer, "Quantitative assessment of the multiplicity of carbon–halogen bonds: Carbenium and halonium ions with F, Cl, Br, and I," J. Phys. Chem. A **118**, 1948–1963 (2014).
[124]E. Kraka, W. Zou, Y. Tao, and M. Freindorf, "Exploring the mechanism of catalysis with the unified reaction valley approach (URVA)—A review," Catalysts **10**, 691 (2020).
[125]E. Kraka and D. Cremer, "Computational analysis of the mechanism of chemical reactions in terms of reaction phases: Hidden intermediates and hidden transition states," Acc. Chem. Res. **43**, 591–601 (2010).
[126]W. Zou, T. Sexton, E. Kraka, M. Freindorf, and D. Cremer, "A new method for describing the mechanism of a chemical reaction based on the unified reaction valley approach," J. Chem. Theory Comput. **12**, 650–663 (2016).
[127]K. Fukui, "The path of chemical reactions—The IRC approach," Acc. Chem. Res. **14**, 363–368 (1981).
[128]H. P. Hratchian and E. Kraka, "Improved predictor–corrector integrators for evaluating reaction path curvature," J. Chem. Theory Comput. **9**, 1481–1488 (2013).
[129]Y. Tao, W. Zou, M. Freindorf, D. Cremer, and E. Kraka, pURVA, Computational and Theoretical Chemistry Group (CATCO), Southern Methodist University, Dallas, TX, 2021.
[130]M. Z. Makoś, M. Freindorf, Y. Tao, and E. Kraka, "Theoretical insights into [NHC]Au(I) catalyzed hydroalkoxylation of allenes: A unified reaction valley approach study," J. Org. Chem. **86**, 5714–5726 (2021).
[131]E. Kraka and M. Freindorf, "Chemical bonding in homogenous catalysis—Seen through the eyes of vibrational spectroscopy," in *Reference Module in Chemistry, Molecular Sciences and Chemical Engineering*, Comprehensive Computational Chemistry (Elsevier, Heidelberg, 2022), pp. 1–27.